# Significantly reduced *c*-axis thermal diffusivity of graphene-based papers

**Meng Han**[1,5] , **Yangsu Xie**[2,5], **Jing Liu**[3], **Jingchao Zhang**[4] **and Xinwei Wang**[1]

[1] Department of Mechanical Engineering, 2010 Black Engineering Building, Iowa State University, Ames, IA 50011, United States of America
[2] College of Chemistry and Environmental Engineering, Shenzhen University, Shenzhen 518055, Guangdong, People's Republic of China
[3] The University of Tokyo, 7-3-1 Hongo, Bunkyo, Tokyo, 113-8656, Japan
[4] Holland Computing Center, University of Nebraska-Lincoln, Lincoln, NE 68588, United States of America

E-mail: xwang3@iastate.edu

## Abstract

Owing to their very high thermal conductivity as well as large surface-to-volume ratio, graphene-based films/papers have been proposed as promising candidates of lightweight thermal interface materials and lateral heat spreaders. In this work, we study the cross-plane (*c*-axis) thermal conductivity ($k_c$) and diffusivity ($\alpha_c$) of two typical graphene-based papers, which are partially reduced graphene paper (PRGP) and graphene oxide paper (GOP), and compare their thermal properties with highly-reduced graphene paper and graphite. The determined $\alpha_c$ of PRGP varies from $(1.02 \pm 0.09) \times 10^{-7} \, \mathrm{m^2 \, s^{-1}}$ at 295 K to $(2.31 \pm 0.18) \times 10^{-7} \, \mathrm{m^2 \, s^{-1}}$ at 12 K. This low $\alpha_c$ is mainly attributed to the strong phonon scattering at the grain boundaries and defect centers due to the small grain sizes and high-level defects. For GOP, $\alpha_c$ varies from $(1.52 \pm 0.05) \times 10^{-7} \, \mathrm{m^2 \, s^{-1}}$ at 295 K to $(2.28 \pm 0.08) \times 10^{-7} \, \mathrm{m^2 \, s^{-1}}$ at 12.5 K. The cross-plane thermal transport of GOP is attributed to the high density of functional groups between carbon layers which provide weak thermal transport tunnels across the layers in the absence of direct energy coupling among layers. This work sheds light on the understanding and optimizing of nanostructure of graphene-based paper-like materials for desired thermal performance.

Keywords: graphene oxide paper, partially reduced graphene paper, thermal conductivity, thermal duffusivity, interlayer spacing, oxygen-contained functional groups

(Some figures may appear in colour only in the online journal)

## 1. Introduction

Nowadays, with the fast development of the integration and miniaturization of energy systems, such as solar cells devices, battery systems, heaters, etc. thermal management becomes one of the most important factors influencing the energy efficiency. Thermal interface resistance and heat spreading are rising problems which promote the demand to search for novel materials with high thermal management performance. Graphene, since its first exfoliation from graphite in 2004 [1],

has attracted extensive attentions due to its extremely high thermal and electrical conductivity and high mechanical strength. Early work shows that graphene has an extremely high thermal conductivity ($\sim$5000 W m$^{-1}$ K$^{-1}$) [2] exceed that of graphite ($\sim$2000 W m$^{-1}$ K$^{-1}$) [3] in the basal plane. Following works find that thermal conductivity of graphene can be strongly suppressed by the low quality of graphene layers and the energy coupling with substrate [4, 5]. Even though, the thermal conductivity of graphene still exceeds those of metals. This high thermal conductivity along with high electrical conductivity, high carrier mobility makes graphene a promising material for the future electronic

---

[5] Equal contribution authors.

devices. Nevertheless, direct use of graphene is still limited by its small scale and the difficulty of mass production.

In recent years, graphene-based materials such as graphene aerogel [6, 7], graphene foam [8, 9], graphene paper (GP) [10, 11] pave a way for the use of the remarkable properties of graphene. Among these, free-standing graphene nanoplates or GP are of great interest. Due to its high potential use in thermal management materials, extensive efforts have been made to study the thermal transport properties of GP. Xiang *et al* [12] prepared graphite nanoplatelet paper from exfoliated graphite nanoplatelets (GNPs) and reported a thermal conductivity of $178 \, \mathrm{W \, m^{-1} \, K^{-1}}$ after mechanical compressing. Similarly, Wu *et al* [13] fabricated a binder-free, self-standing flexible paper from GNPs, and reported a thermal conductivity of $313 \, \mathrm{W \, m^{-1} \, K^{-1}}$ after the annealing process. Malekpour *et al* [14] employed an opto-thermal Raman measurement on a set of graphene laminates with a thickness from 9 to $44 \, \mu\mathrm{m}$ deposited on PET and reported a thermal conductivity ranging from 40 to $90 \, \mathrm{W \, m^{-1} \, K^{-1}}$ at room temperature (RT). This study shows that the average size and alignment of graphene flakes are of key parameters defining the thermal conduction in graphene laminate. Xin *et al* [10] reported the fabrication of a highly ordered large-area freestanding GP by direct electro-spray of graphene films with a continuous roll-to-roll process. The reported thermal conductivity can reach $1238 \, \mathrm{W \, m^{-1} \, K^{-1}}$ at RT after annealing at $2200 \, °\mathrm{C}$. Song *et al* [15] investigated the structural evolution of a thermally reduced graphene oxide (rGO) film by annealing at different temperatures. It is reported that an ultrahigh thermal conductivity of $1044 \, \mathrm{W \, m^{-1} \, K^{-1}}$ is obtained after annealing at $1200 \, °\mathrm{C}$ and a critical temperature of $1000 \, °\mathrm{C}$ is required for significant improvement of thermal conductivity.

Due to the difficulty in measuring the cross-plane thermal conductivity of such thin films, most of the previous work focused on the in-plane thermal properties, although the cross-plane thermal properties are the most significant factors for thermal interface materials. Our recent work reported a novel method for the measurements of the in-plane ($k_a$) and cross-plane ($k_c$) thermal conductivity of a highly reduced ($-99\%$ carbon) and highly-oriented GP from RT down to very low temperatures [16, 17]. $k_a$ shows an interesting jump from $529 \, \mathrm{W \, m^{-1} \, K^{-1}}$ at 270 K to $3013 \, \mathrm{W \, m^{-1} \, K^{-1}}$ at 245 K. $k_c$ varies with temperature and has a peak at about 80 K, similar as that of graphite reported by Fu *et al* [18] and Zhang *et al* [19]. At RT, $k_c$ is $6.08 \, \mathrm{W \, m^{-1} \, K^{-1}}$, nearly two orders of magnitude smaller than that of $k_a$ ($529 \, \mathrm{W \, m^{-1} \, K^{-1}}$ before switch-on). Due to the different reduction methods and reduction conditions, the electrical and thermal properties of rGO highly depend on the level of reduction of oxidation groups and restoration of $sp^2$ carbon–carbon bonds. Recent work by Renteria *et al* [11] prepared graphene oxide films by the modified Hummer's method and reduced with a thermal annealing treatment at different temperatures. Both $k_a$ and $k_c$ were measured before and after the annealing processes under different temperatures. $k_a$ increases from 3 to $61 \, \mathrm{W \, m^{-1} \, K^{-1}}$ at RT by the annealing treatment, indicating the quality improvement of the graphene clusters in the sample. $k_c$ revealed an interesting decrease from $0.2 \, \mathrm{W \, m^{-1} \, K^{-1}}$ to only $0.09 \, \mathrm{W \, m^{-1} \, K^{-1}}$. The authors attributed the decrease of $k_c$ to the formation of air pockets during the annealing process, by assuming that the intrinsic cross-plane thermal transport properties have no change during the annealing process. This is, however, not usually the case, and need to be taken into further consideration.

In this work, we report the measurements on the thermal conductivity and diffusivity of partially reduced GP and graphene oxide paper (GOP) in the cross-plane direction. Based on a pulsed laser-assisted thermal relaxation 2 (PLTR2) technique, the measurement can be taken from RT down to 10 K. Combined with the structure characterization by Raman spectroscopy, x-ray diffraction (XRD), and energy-dispersive x-ray spectroscopy (EDS), the unique thermal transport properties in PRGP and GOP are attributed to the interlayer spacing, the arrangement of the flakes and the chemical compositions in these graphene-based materials. A systematic and detailed analysis of the nanostructures and the thermal behaviors of the three graphene-based papers including GP, PRGP, and GOP is presented in the result section.

## 2. Experimental details

The PLTR2 technique is used to investigate the thermal transport properties of PRGP and GOP in the cross-plane direction. Our samples are very thin (tens of $\mu\mathrm{m}$). Although the nanosecond laser flash method can be used for measuring the cross-plane thermal diffusivity ($\alpha_c$) of such samples at RT, at very low temperatures, the backside radiation has a wavelength in the order of a few 0.1 mm. This makes the thermal response measurement extremely challenging and difficult using the radiation method at very low temperatures. Our PLTR2 technique is designed to overcome this challenge and measure the cross-plane thermal conductivity/diffusivity down to very low temperatures. In the PLTR2 measurement, an iridium (Ir) coating on the back surface of the sample is fed with a DC current and acts as the temperature sensor. For PRGP, as a good conductor (conductivity $\sim 5 \times 10^3 \, \mathrm{Sm^{-1}}$) [16], we need to isolate it from the Ir coating. While for GOP, as an isolator with extremely high electrical resistivity, there is no need to be insulated from the Ir coating. In this case, the Ir coating will be directly coated on the back surface of GOP for temperature sensing. More details of the PLTR2 technique can be found in our past work [17].

### 2.1. Sample preparation

The PRGP and GOP samples are purchased from ACS materials. Briefly, GOP is composed of graphene oxide flakes stacking layer by layer. PRGP is obtained by partly reducing GOP, and GP is obtained by highly reducing GOP. Thus, the structure difference among the three materials represents three typical stages in the reduction process. According to the technical data sheet, they are produced in the following
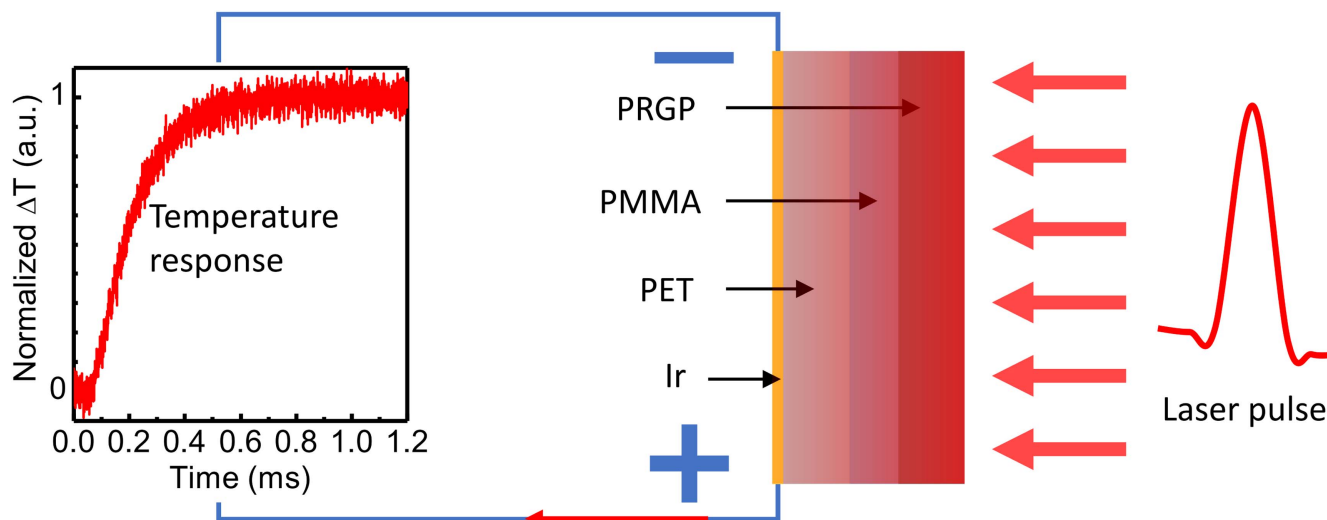
**Figure 1.** Schematic of the structured sample under the PLTR2 measurement. The multilayered sample is prepared by attaching PRGP to a PET film with PMMA/toluene solution. The Ir coating is first sputtering coated on the other side of the PET film before the attachment. During the measurement, a DC current is fed through the Ir coating and the temperature response of the multilayered sample at the back surface after the laser pulse heating is detected by the electrical resistance or voltage variation of the Ir coating.

process. First, the graphite oxide is prepared from graphite by using the modified Hummer's Method [20, 21]. Then a suspension of graphene oxide (GO) sheets is obtained through the sonication and exfoliation of the prepared graphite oxide [22]. The free-standing GOP is assembled in direct flow (typically by vacuum assisted flow-filtration), which can be chemically reduced to produce PRGP. Here for PRGP, we use a 0.5 $\mu$m thick PET film to separate it from the Ir coating to fulfill the PLTR2 requirement. Figure 1 (right) shows the multilayered sample prepared for the PLTR2 measurement. First, the PET film is sputtering coated with 20 nm Ir within a specific area similar to the lateral size of the PRGP sample. Then the PRGP sample is attached to the uncoated side of the PET film with a PMMA/toluene solution. The PMMA/toluene solution is prepared by dissolving PMMA particles in toluene solvent with a mass percentage of 1%. After the attachment, the sample is placed in a fume hood and heated at 50 °C for several hours. The toluene solvent will volatilize and good attachment between PET, PMMA and PRGP forms. Then the multilayered PRGP/PMMA/PET/Ir sample is suspended between two electrodes with the Ir coating facing the electrodes to form an electric circuit. In this step, silver paste is used to enhance the electrical and thermal contacts between the Ir coating and the electrodes. Note that, during the sample preparation, the most important and challenging thing is to make sure the PRGP is well isolated from the Ir coating, which means only the Ir coating is in the electric circuit to act as a temperature response detector. For GOP, the sample preparation is similar but much easier. The Ir is directly coated on the back surface of the sample, no PET or PMMA film is needed.

### 2.2. Structure characterization

The scanning electron microscope (SEM) is first employed to investigate the alignment and orientation of GO or rGO flakes

in GOP and PRGP. Figure 2 shows the SEM images of GOP and PRGP, as well as GP for comparison, all with the top view and cross-section view. From figure 2(a), we can see that the surface of GOP is covered with unordered wrinkles. PRGP also has the similar surface morphology (figure 2(b)), but the wrinkles are smaller. Not like GOP or PRGP, the surface of GP is smooth, where the edges of graphene flakes are sharp and clear (figure 2(c)). The cross-sections are obtained by directly tearing the samples apart and are therefore not very smooth. The layered structure and the alignments of GO or rGO flakes in GOP and PRGP can be seen clearly in figures 2(d) and (e). Compared to the SEM images of GPs under molecular level modifications in recent work [23], our GOP and PRGP are denser. There is no evidence of large air-pockets in GOP or PRGP, ensuring that the two samples are close to fully dense. The teared edge of GP is relatively sharp, and the graphene flakes are fully dense in the structure (figure 2(f)), similar to those of bulk graphite [19].

The quality and thermal stability of GOP and PRGP are then investigated by using the thermogravimetric analysis (TGA) technique. Figure 3(a) shows the weight loss curve (blue) and the first derivative of the weight loss (DTG) curve (red) of GOP. The weight loss up to 100 °C is due to the desorption of physically adsorbed water. The following sharp drop from about 100 °C to 300 °C with a peak at about 200 °C takes more than 30% of the original weight. This weight loss is attributed to the decomposition of labile functional groups, which have also been found in the TGA characterization of GO in previous work [24–26]. The small differences in the peak positions (200 °C, 220 °C, and 230 °C, respectively) may be due to different methods in obtaining GO from graphite or the errors in the temperature detecting. Figure 3(b) shows the TGA results of PRGP. The weight loss up to 100 °C is much less than that of GOP, meaning the PRGP contains much less water. There is also a similar sharp weight
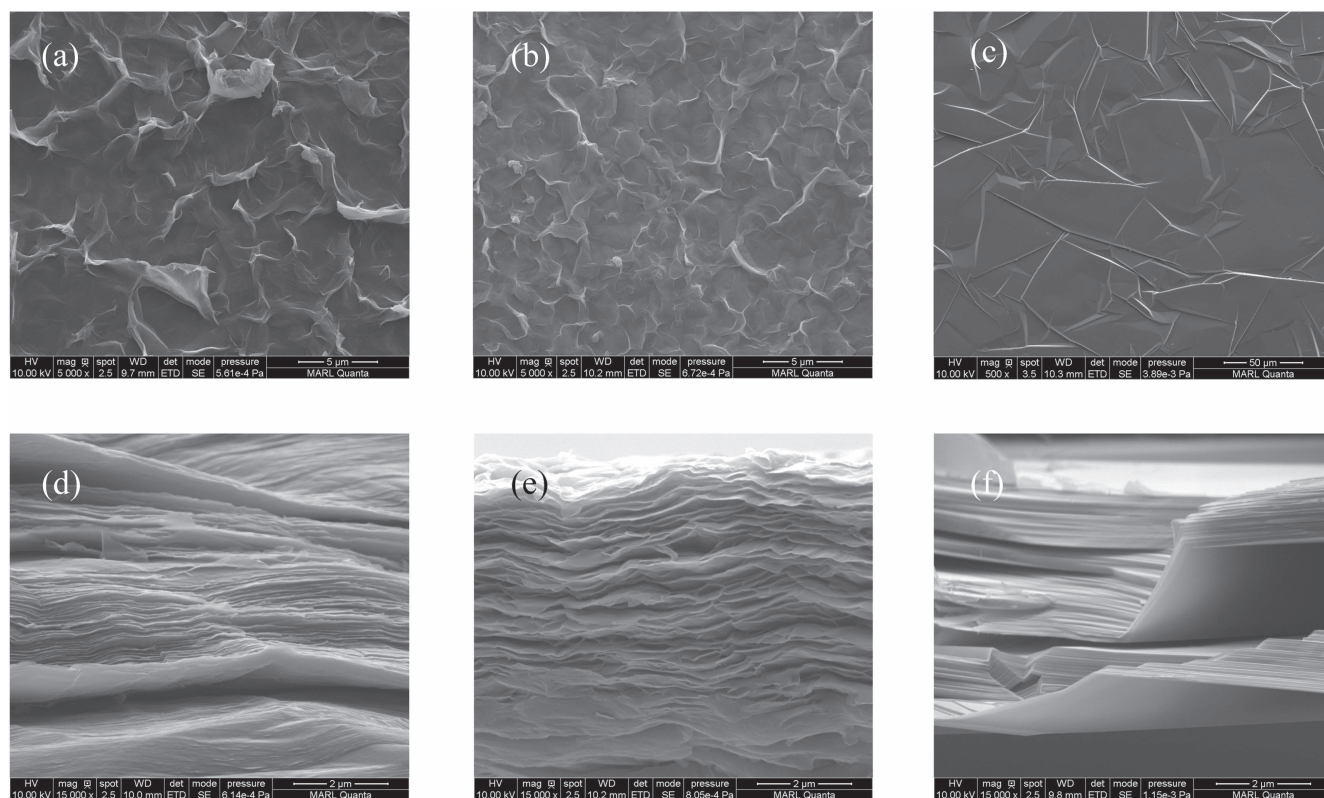
**Figure 2.** SEM images of GOP, PRGP and GP. (a)–(c) The top views of GOP, PRGP and GP, respectively. (d)–(f) The cross-section views of GOP, PRGP and GP, respectively.

loss at around 200 °C, due to the removal of the labile functional groups.

The structure of PRGP and GOP is further characterized by using the XRD and Raman spectroscopy. The blue curve in figure 3(c) shows the XRD pattern of GOP. We can see the peak is located at 10.52°, corresponding to the (002) crystal plane of GOP. The interlayer spacing is determined at 8.4 Å which is consistent with 8.32 Å at 10.6° for graphene oxide from literature [27, 28]. The large interlayer spacing has been attributed to the formation of oxygen-contained functional groups like hydroxyl, epoxy, and carboxyl groups [29], especially the hydroxyl and epoxy forms on the basal plane. The crystallite size is calculated at 7.1 nm, much smaller than that of GP in our previous work [17]. The red curve in figure 3(c) shows the XRD pattern of PRGP. A relatively lower peak is located at 24.15°, corresponding to the (002) plane of reduced graphene materials. The interlayer spacing is determined at 3.68 Å, about 10% percent larger than 3.35 Å of that of GP and graphite. This indicates that there are just a few remaining functional groups on the basal plane or among the interlayers after chemical reduction. The crystallite size is calculated at 4.8 nm, even smaller than that of GOP. The relatively wider and lower peak of PRGP indicates that the crystalline structure of PRGP is not as good as that of GOP.

Figure 3(d) shows the Raman spectra of PRGP and GOP, as well as that of GP studied in our previous work for comparison purpose [17]. We can see two intense peaks from the red curve of PRGP, where the D peak at around 1345 cm$^{-1}$ is attributed to a finite crystal size effect and the G peak at around 1579 cm$^{-1}$ is due to the first-order scattering of the $E_{2g}$ mode. For GOP, these two peaks are located at 1347 and 1591 cm$^{-1}$ (blue curve). The intensity ratio of the D peak to G peak ($I_D/I_G$) is getting larger from GOP to PRGP (mainly due to the increase of the D peak intensity), which has been commonly reported for rGO from chemical reduction of GO [29–31]. This increase of $I_D/I_G$ from GOP to PRGP suggests a further decrease in the size of sp$^2$ domains upon chemical reduction of GOP [30, 32]. This can be explained by the loss of carbon atoms from the graphene lattice which results in the formation of defects such as vacancies and distortions, where the integrated sp$^2$ domains are further separated into smaller ones [24]. Further reduction is likely to induce the decrease of $I_D/I_G$, due to the recovery of the sp$^2$-hybridized C–C bonds [25, 33, 34]. The peak at around 1950 cm$^{-1}$ is not from the samples and is always there in our Raman system. It may be fluorescence signal, or due to the light source, or some other noise from the Raman system. The 2D peak of GP at about 2700 cm$^{-1}$ is relatively sharp and intense, which is consistent with that of high-quality multilayered graphene and graphite [35]. While in GOP, this peak is very weak and is highly broadened, indicating the high defect level. In PRGP the 2D peak is still weak, but relatively higher than that of GOP, due to the better graphitization after chemical reduction. The S3 peak at 2900 cm$^{-1}$ is invisible in GP, and becomes larger from GOP to PRGP, also an indicator of better graphitization in PRGP than in GOP [36].

The chemical compositions of GP, PRGP, and GOP are studied by the EDS technique, from which the atomic
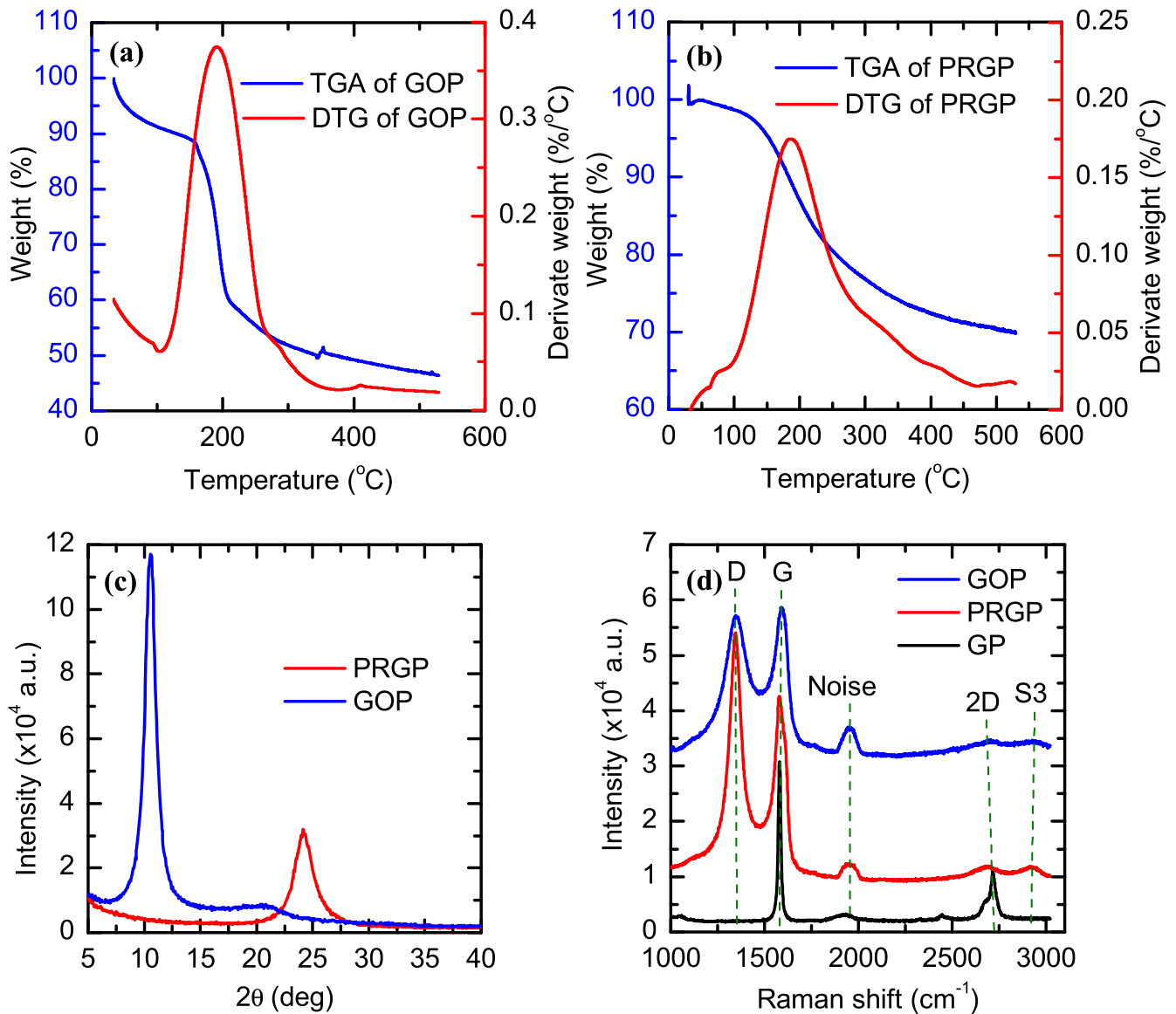
**Figure 3.** Sample characterization (a) TGA and DTG signals of GOP; (b) TGA and DTG signals of PRGP; (c) XRD signal of PRGP and GOP; (d) Raman spectra of GP, PRGP and GOP.

fractions of existing elements in these materials are determined. For GP, the atomic fraction is C (99.81%) and O (0.19%). For PRGP, the atomic fraction is C (86.43%), O (9.93%) and I (3.65%), shows relatively high ratio of O. For GOP, the atomic fraction is C (63.74%), O (35.12%), S (1.01%), and K (0.14%), indicates large amount of O in it. The x-ray photoelectron spectroscopy (XPS) has also been performed on the three samples in our recent work [16]. Here we only summarize the results. The resulting elemental composition of GP is C 1s (98.91%), O 1s (0.66%), and F 1s (0.43%). In PRGP, the chemical bond includes C 1s (68.9%), O 1s (25.10%), N 1s (2.50%), Fe 2p (1.98%) and I 3d (1.51%). While in GOP, the chemical bond composition is C 1s (61.76%), O 1s (34.40%), Au 4f (1.13%), F 1s (1.63%), and Fe 2p (1.07%). The different chemical compositions in the EDS and XPS results are mainly due to the relative depth of analysis of the two techniques. EDS provides information on elements concentration in the 'bulk' sample, while XPS

probes the chemical composition at the near surface (only the top several nm) of the sample. This can help explain the more minor elements and the relatively higher O fractions in GOP and GP from the XPS results. The significantly higher O fraction in PRGP from the XPS results may come from the lower chemical reduction level at the sample surface. Despite those differences from the two techniques, the C to O ratio clearly increases from GOP to PRGP and to GP.

### 2.3. Experimental setup and physical model

The PLTR2 measurement is performed in a vacuum chamber with a pressure lower than 0.6 mTorr to reduce the heat convection from the sample surface. Figure 4 shows the schematic of the experimental setup. The sample is held vertically on a copper substrate which is specifically designed for horizontal laser irradiation from outside. The experimental temperature is controlled through the cooling head under the
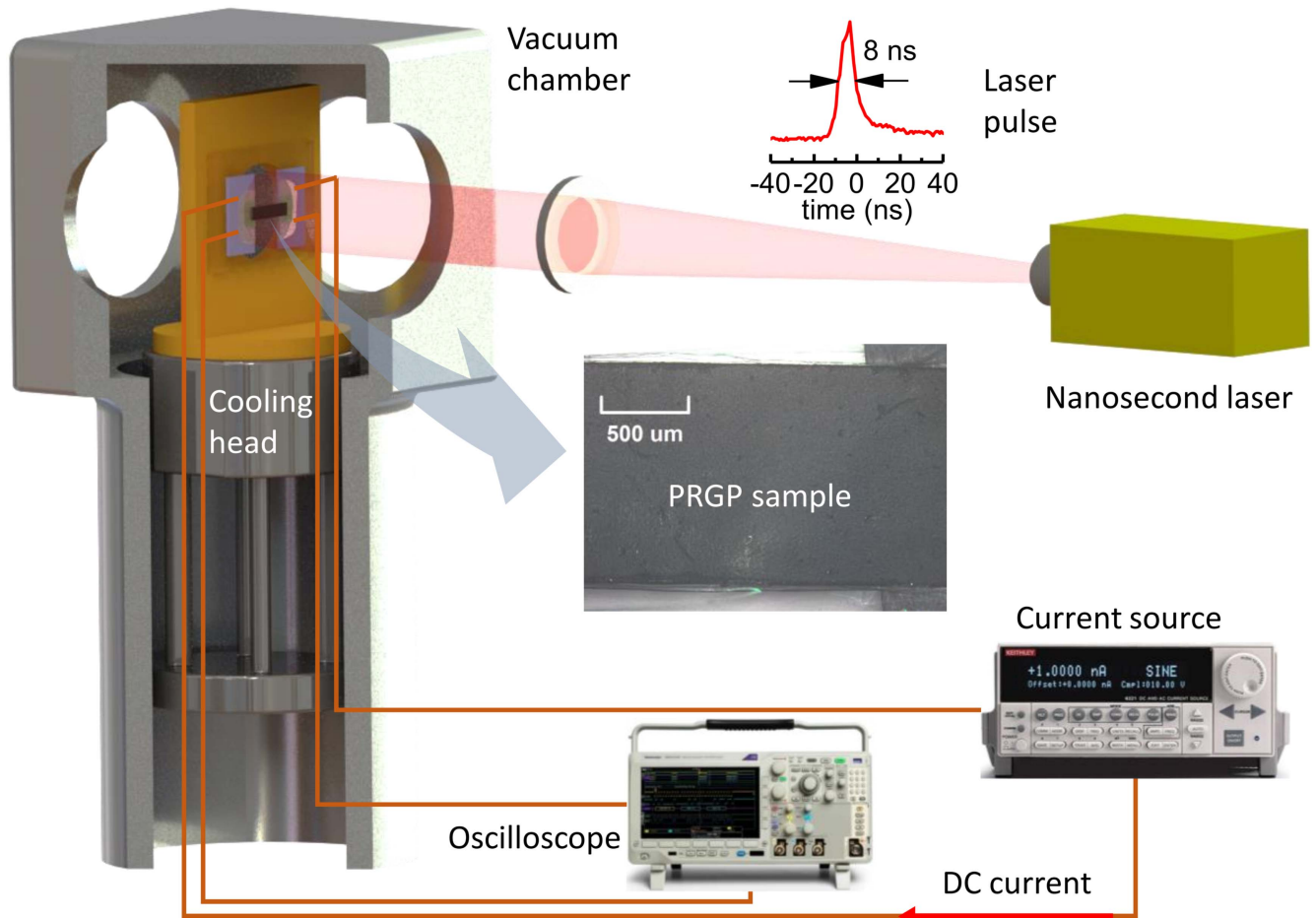
**Figure 4.** Schematic of the experimental setup (not to scale). The insets show the pulse laser duration (left-up) and the microscope image of the PRGP/PMMA/PET/Ir sample (central).

substrate by a Janis closed cycle refrigerator (CCR) system. This CCR system can provide stable temperature from RT down to 10 K with an accuracy of 0.5 K. To make sure the sample reaches the controlled temperature, we wait for about 40 min after each set of the experimental temperature. The sample is connected to a current source (Keithley 6221) and an oscilloscope (Tektronix MDO 3052), where a circuit forms through the Ir coating.

During the measurement, a DC current is fed to the sample through the Ir coating and the electrical resistance or voltage evolutions are monitored by the oscilloscope. A nanosecond laser irradiates the front surface of the sample and thermal transport occurs in the sample. After a single laser pulse, the temperature of the Ir coating will increase from the initial experimental temperature to a maximum value and then decrease as heat dissipates to the substrate. This temperature evolution will be reflected in the electrical resistance or voltage variations of the Ir coating. The insets in figure 4 show the laser pulse width and a microscopic image of the PRGP/PMMA/PET/Ir sample. The laser pulse width is about 8 ns, more than four orders of magnitude smaller than the characteristic thermal relaxation time ($t_c$) of our PRGP and GOP samples in the cross-plane direction. Thus, the finite pulse duration effect is negligible. A silicon photodiode is

connected to the oscilloscope to capture the laser pulse and the position of the laser pulse in the time scale is taken as the beginning time of the thermal relaxation which is of crucial importance in the PLTR2 model. The original laser spot size is about 3.5 cm, much larger than the lateral dimensions of the PRGP and GOP sample (with a length shorter than 3 mm). Thus, we can safely assume a uniform laser energy distribution at the front surface of the sample (take an optical absorption depth of 31 nm from that of graphite). With a cover (not shown in figure 4) before the sample, we also make sure that only the suspended part of the sample is irradiated, and that the disturbance from the laser heating on the electrodes and the wirings is reduced to a negligible level.

In the real case, thermal energy will dissipate in all directions simultaneously. While in the present measurements, the thermal transport can be simplified as one-dimensional in the cross-plane direction and then in the in-plane direction, due to the large difference in thermal characteristic time or characteristic length in these two directions. According to our recent work [16], the in-plane thermal diffusivity ($\alpha_a$) of PRGP is no larger than $2.5 \times 10^{-6}$ m$^2$ s$^{-1}$, which corresponds to a $t_c$ larger than 2.5 s. While in the cross-plane direction, $t_c$ is no larger than 1 ms (shown in figure 5(b)), more than 3 orders of magnitude smaller than that in the in-plane direction. Thus, the
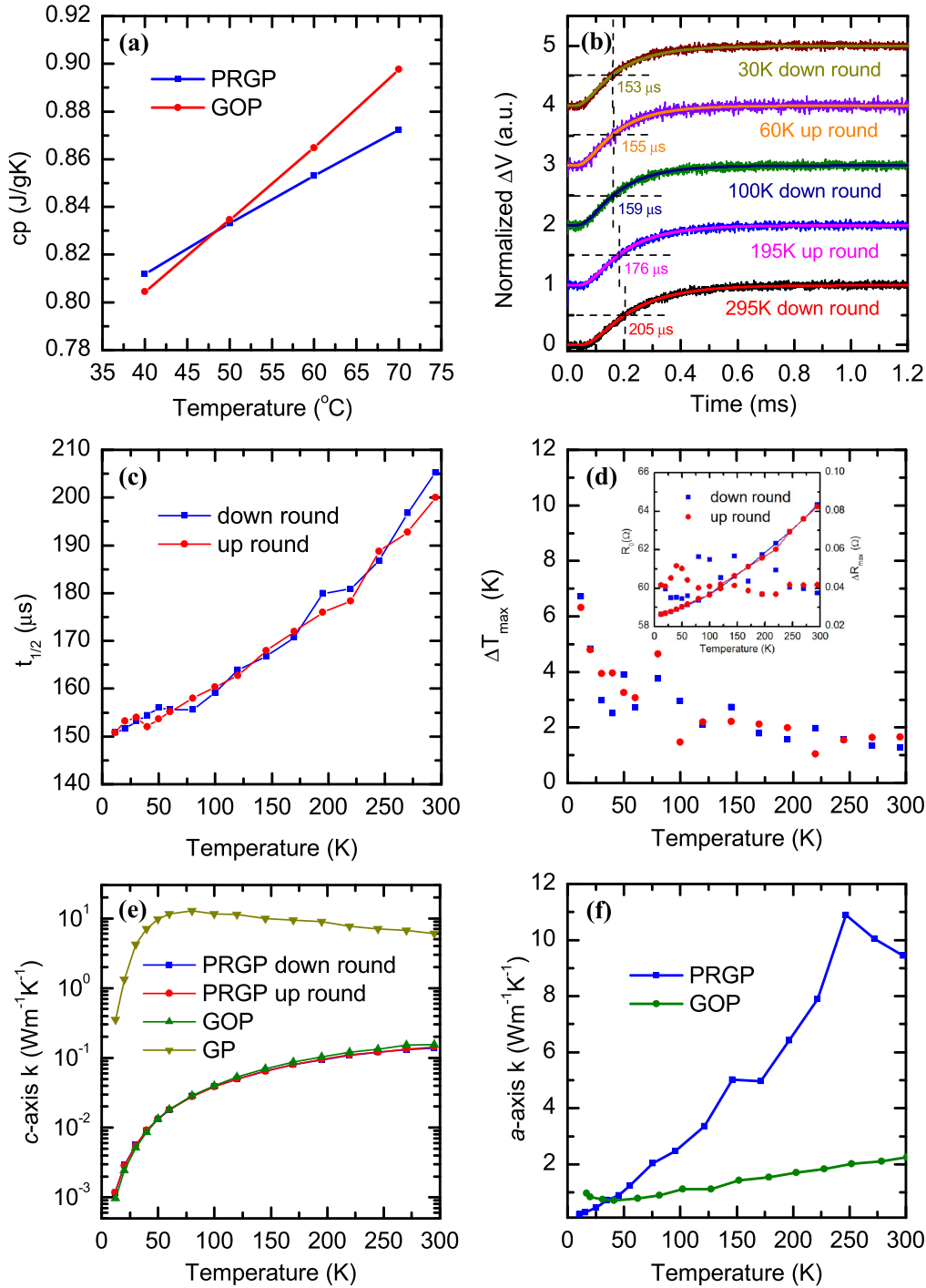
**Figure 5.** Thermal transport characterization. (a) DSC characterization of the $c_p$ of PRGP and GOP at near RT. (b) Normalized voltage variations and the best fitting curves at several of our environmental temperatures for PRGP. Also shown are the half rise times at these temperatures. (c) $t_{1/2}$ versus temperature of PRGP. (d) Maximum temperature rises during a single measurement against the environmental temperature. The inset shows the initial electrical resistance and the according maximum resistance change against the environmental temperature. (e) *c*-axis thermal conductivity of PRGP and GOP, as well as GP studied in our recent work. Reprinted from [17], Copyright (2018) with permission from Elsevier. (f) *a*-axis thermal conductivity of PRGP and GOP determined in our previous work. Reproduced from [16] with permission of The Royal Society of Chemistry.

1D thermal transport simplification is valid. As for GOP, $k_a$ and $\alpha_a$ have also been characterized in our recent work [16]. The corresponding in-plane $t_c$ is larger than 0.5 s even at very low temperatures. While in the cross-plane direction, $t_c$ is no larger than 2 ms, still orders of magnitude smaller than that in the in-plane direction.

The governing equation for the 1D thermal transport in a multilayered film can be expressed as follows [37]:

$$\frac{\partial T_i(x, t)}{\partial t} = \alpha_i \frac{\partial^2 T_i(x, t)}{\partial x^2}, \ i = 1, \ 2, \ 3, \cdots \quad (1)$$

For a single-layered film, such as GOP with no PMMA or PET attached and the thickness of Ir coating can be neglected, the governing equation can be solved by using the Green's function and expressed as the following equation:

$$T(x, t) = \frac{Q}{\rho c_p L} \left[ 1 + 2 \sum_{m=1}^{\infty} \frac{\sin(m\pi\tau_{opt}/L)}{m\pi\tau_{opt}/L} \times \cos\left(\frac{m\pi x}{L}\right) \times \exp\left(\frac{-m^2\pi^2}{L^2}\alpha t\right) \right]. \quad (2a)$$

At the rear surface where $x = L$, the temperature evolution can be expressed by:

$$T(L, t) = \frac{Q}{\rho c_p L} \left[ 1 + 2 \sum_{m=1}^{\infty} (-1)^m \frac{\sin(m\pi\tau_{opt}/L)}{m\pi\tau_{opt}/L} \times \exp\left(\frac{-m^2\pi^2}{L^2}\alpha t\right) \right]. \quad (2b)$$

When normalized from the initial temperature to the maximum temperature, we have:

$$T^*(L, t) = 1 + 2 \sum_{m=1}^{\infty} (-1)^m \frac{\sin(m\pi\tau_{opt}/L)}{m\pi\tau_{opt}/L} \times \exp\left(\frac{-m^2\pi^2}{L^2}\alpha t\right). \quad (2c)$$

In a small temperature range, the electrical resistance of Ir is linearly proportional to the temperature as $R = (\rho_0 + \gamma \cdot \Delta T) \times (l/A_c)$, where $\rho_0$ is the initial electrical resistivity at the experimental temperature, $\gamma$ the local temperature coefficient of electrical resistivity, $\Delta T$ the temperature rise, $l$ length of the sample, $A_c$ cross-section area of the Ir coating. When normalizing $R$ from the initial value ($R_0$) before the laser pulse to the maximum value ($R_m$) after the laser pulse, we have

$$R^* = \frac{R - R_0}{R_m - R_0} = \frac{\Delta R}{\Delta R_m} = \frac{\Delta T}{\Delta T_m} = T^*. \quad (3)$$

Thus, the temperature response of the rear surface of our samples can be directly detected by the electrical resistance or voltage evolutions with an oscilloscope (the response curve shape is shown in figure 1). The thermal diffusivity of a single-layered sample can be directly calculated from the half rise time ($t_{1/2}$) of the response curve as $\alpha = (1.37L^2/\pi^2 t_{1/2})$ [38]. Then the thermal conductivity can be calculated by $k = \alpha \cdot \rho \cdot c_p$ with the given density and specific heat of the material.

For multilayered composites, such as the PRGP/PMMA/PET/Ir sample here, the relations between the temperature response and the electrical resistance variation also hold true. Analytical solutions of 1D thermal transport in multilayered composites based on the laser flash method have also been derived in detail [37, 39]. However, these solutions are usually complicated. In this work, we use a numerical method to simulate the 1D thermal transport in the PRGP/PMMA/PET/Ir multilayered sample and fit the extracted rear surface temperature response curves with that from the experimental data, both after normalization. In the numerical simulation, the thicknesses of the layers are key parameters which should be determined ahead of PLTR2 measurement. The thickness of PRGP is determined at $11.5 \pm 0.5\ \mu m$ with a micrometer. Also, the weight of a piece of PRGP with a lateral dimension of $3.366 \times 1.895\ mm^2$ is measured at $142\ \mu g$ with a microbalance. Thus, the density of PRGP is calculated at $1.936 \pm 0.085\ g\,cm^{-3}$, a little smaller than the full density of pristine graphite ($2.21\ g\,cm^{-3}$). This relatively lower density is mainly due to the larger interlayer spacing than graphite as determined by the XRD in the last section. Another reason is the disordered alignments of the rGO flakes, which leads to large spacing among flakes and hence reduces the density of the structure. Therefore, we can conclude that the PRGP is to some extent a full density graphene-based structure. The thickness of our multilayered PRGP/PMMA/PET/Ir sample is measured at $12 \pm 0.5\ \mu m$ with the micrometer. The thickness of PET is taken as $0.5\ \mu m$ (the production description which is also confirmed in our recent work [17]). The microbalance is used to measure the weight of the multilayered sample after the PLTR2 measurement. The total weight of the multilayered sample is determined at $102\ \mu g$. With the lateral dimensions of the multilayered sample and the Ir coating determined at $2.95 \times 1.47\ mm^2$ and $2.95 \times 1.20\ mm^2$ under the microscope, the thickness of the PMMA is calculated at $0.2\ \mu m$. Similarly, the thickness and density of GOP are determined with the help of the micrometer and microbalance, which are $28.5 \pm 0.5\ \mu m$ and $1.465 \pm 0.027\ g\,cm^{-3}$, respectively.

The densities, heat capacities of the PMMA and PET are taken from literature[40, 41]. The heat capacity of PRGP is taken from that of graphite [42], which is always an assumption in the literature [43, 44]. To confirm this, the specific heat of our PRGP and GOP samples is measured by the differential scanning calorimetry (DSC) within a Netzsch STA449F1 TDA/DSC system. The measurement is taken from 35 °C to 75 °C, which is the lowest available range in our TDA/DSC system and makes sure that the PRGP and GOP are not destructed or further reduced thermally. The results are shown in figure 5(a), from which we can see $c_p$ of PRGP increases linearly along with the temperature in the measurement temperature range, consistent with that of graphite [45]. Thus, we can safely extract $c_p$ of PRGP at RT (22 °C), which is $776\ J\,g^{-1}\,K^{-1}$, about 10% higher than that of graphite. Considering the uncertainty of the TGA/DSC measurement, this difference is not significant. Also shown in figure 5(a) is $c_p$ of GOP determined from the DSC measurement, which also has no significant difference from those of our PRGP sample and graphite. Thus, during the data processing in this work, $c_p$ of PRGP and GOP are taken from that of graphite. The influence of the deviations of $c_p$ on $k_c$ and $\alpha_c$ of PRGP and GOP will be discussed later. $k_c$ of PMMA and PET are also taken from literature [46–48]. Thus, in the 1D heat transfer model of the multilayered PRGP/PMMA/PET/Ir sample, the only unknown parameter is $k_c$ of

PRGP. With these known parameters and trial values of $k_c$, different temperature response curves of the sample backside can be obtained. Then the least square method is used to extract the one that gives the best fit to the experimental data. For GOP, the thermal diffusivity can be directly extracted from the half rise time as described before.

## 3. Results and discussion

### 3.1. Thermal conductivity variation against temperature

The PLTR2 measurements are performed every 25 K from 295 to 120 K, then every 20 K from 120 to 60 K and finally every 10 K from 60 K to nearly 10 K. Denser data points are collected at low temperatures to monitor the low-temperature effects. For the PRGP sample, the PLTR2 experiment is taken from 295 to 12 K (down round) and then back to 295 K (up round) to study the influence of low-temperature on the structure and thermal transport properties. Figure 5(b) shows the normalized back surface temperature response curves at several of our experimental temperatures. The normalized temperature rises to the maximum value and keeps for a while before decreasing as heat dissipates in the in-plane direction. This proves the validation of the 1D thermal transport simplification. Also shown in figure 5(b) are the corresponding best fitting curves and the half rise times at the specified environmental temperatures. The theoretical curves match with the experimental ones very well. $t_{1/2}$ is a direct indicator of how fast heat transfers in the cross-plane direction, although it cannot be used directly to calculate the thermal diffusivity for multilayered samples. Figure 5(c) shows the variation of $t_{1/2}$ versus temperature, which has no significant difference from the down round to the up round at a given temperature, indicating the small structure change from the low-temperature process. $t_{1/2}$ does not decrease too much from RT to 12 K, not like the rapid decrease of GP studied in our previous work [17]. This reveals the different cross-plane heat transfer behavior of PRGP and GP along with temperature, which will be discussed later.

As described before, in a small temperature range, $R = (\rho_0 + \gamma \cdot \Delta T)(l/A_c) = R_0 + \beta \cdot \Delta T$, with $\beta$ the local temperature coefficient of the electrical resistance, shown in the inset of figure 5(d). Also shown in the inset of figure 5(d) is the maximum electrical resistance rise ($\Delta R_{max}$) after the laser pulse. Thus, with $\beta$ and $\Delta R_{max}$ during a single measurement, the corresponding maximum rear surface temperature rise ($\Delta T_{max}$) can be calculated. Figure 5(d) shows $\Delta T_{max}$ during a single measurement of the experimental temperature, which increases gradually as temperature decreases, especially after 100 K. This is due to the decrease of $\beta$ as shown in the inset in figure 5(d). In the PLTR2 measurements, to keep the lowest temperature rise while providing sufficient signal to noise ratio, $\Delta R_{max}$ is controlled at around 0.5 $\Omega$. In this case, as $\beta$ is getting smaller at lower experimental temperatures, the temperature rises should be larger. Even though, $\Delta T_{max}$ is no larger than 7 K, especially at

a temperature higher than 100 K, it is smaller than 3 K. With such small temperature rises, the physical properties change during a single measurement is negligible.

By least square fitting of the simulation curves to the experimental ones, $k_c$ of PRGP is obtained at all the experimental temperatures. Figure 5(e) shows the extracted $k_c$ of PRGP from RT down to 12 K. Also shown in figure 5(e) is $k_c$ of GOP calculated from the PLTR2 measurement results. For PRGP, $k_c$ decreases from 0.14 W m$^{-1}$ K$^{-1}$ at 295 K to $1.2 \times 10^{-3}$ W m$^{-1}$ K$^{-1}$ at 12 K. This $k_c$ and temperature relationship shows kind of amorphous-like behavior, and is much different from that of GP (see figure 5(e)) studied in our previous work [17]. For GP, $k_c$ increases from 6.08 W m$^{-1}$ K$^{-1}$ at 295 K to 12.8 W m$^{-1}$ K$^{-1}$ at 80 K and then decrease rapidly to 0.35 W m$^{-1}$ K$^{-1}$ at 12.3 K, showing a peak at around 80 K. This difference of $k_c$ evolution with temperature is attributed to the high-level defects and structure disorders in PRGP where the thermal transport ability is mainly limited by the defect and grain boundary scattering in the full experimental temperature range. While for GP, with low-level defects, the Umklapp phonon-phonon scattering dominates at high temperatures which are overridden by the structure defects and related phonon scattering at low temperatures. For GOP, $k_c$ decreases from 0.16 W m$^{-1}$ K$^{-1}$ at 295 K to $9.7 \times 10^{-4}$ W m$^{-1}$ K$^{-1}$ at 12.5 K, very close to those of PRGP.

For comparison, $k_a$ of PRGP and GOP studied in our previous work [16] is shown in figure 5(f). $k_a$ of PRGP changes from 9.4 W m$^{-1}$ K$^{-1}$ at 300 K to 0.14 W m$^{-1}$ K$^{-1}$ at 15 K, showing a decrease trend, despite the small increase from 300 to 250 K. This small increase at relatively high temperature may be due to the U-scattering which gets weaker and will be overridden by the high defect scattering as temperature goes down. Not like the U-scattering mechanism, the defect induced phonon scattering changes little with temperature. The decrease of $k_a$ at low temperature is mainly due to the reduction of occupied phono modes, which are less active at low temperature and are reflected by the rapid decrease of heat capacity as temperature goes down. $k_a$ of GOP decreases from 2.15 W m$^{-1}$ K$^{-1}$ at 306 K to 0.73 W m$^{-1}$ K$^{-1}$ at 37 K which stays almost stable after 69 K with a smaller increase from 25 K.

Recent work by Renteria *et al* [11] reported a much low $k_c$ (0.09 W m$^{-1}$ K$^{-1}$) of rGOP after thermal annealing treatment at 1000 °C, only half of its corresponding original GOP (0.18 W m$^{-1}$ K$^{-1}$) before annealing. Their low $k_c$ of rGOP was simply attributed to the air pockets formed during the annealing treatment, by assuming that the intrinsic $k_c$ has no change from their GOP to rGOP, which is however not usually the case. Besides, due to the large anisotropy of thermal conductivity of this rGOP (60 W m$^{-1}$ K$^{-1}$ in the in-plane), the Maxwell–Garnet's approximation used in their calculation could introduce large errors in the results. Not like the rGOP sample studied in Renteria's work, the PRGP in the present work is close to full density. The SEM images in figure 2(e) also shows layered structure with no significant evidence of air pockets involved in the material. Thus, we believe that the determined $k_c$ is an intrinsic property of the
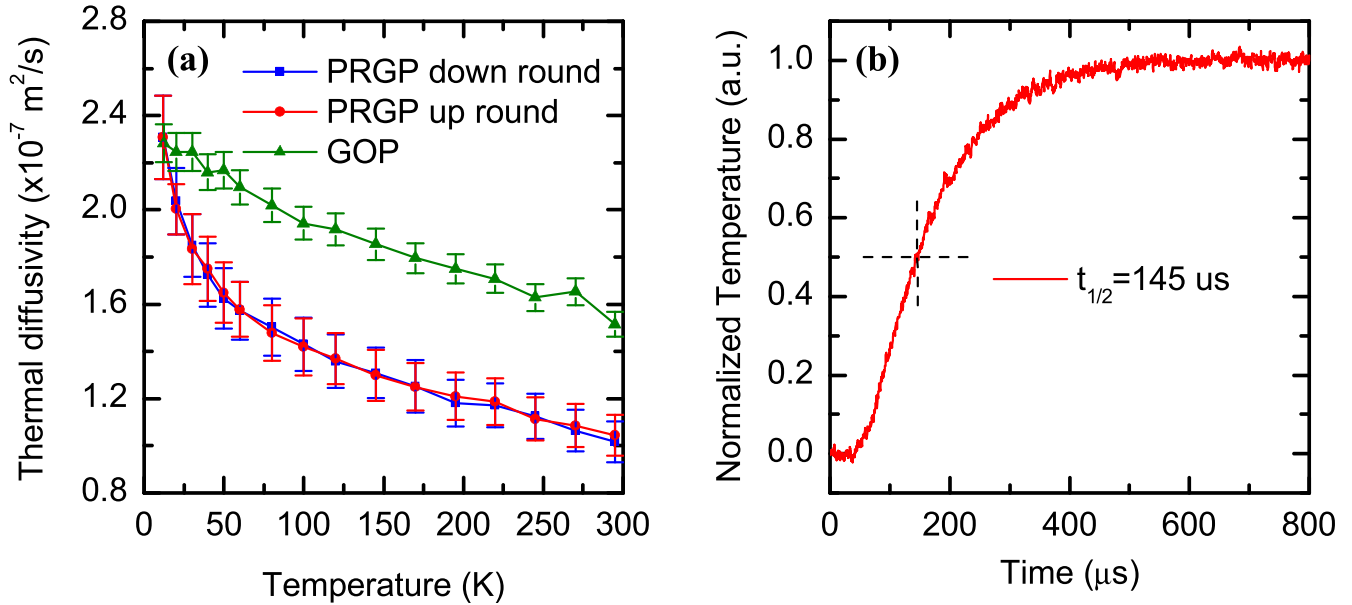
**Figure 6.** (a) *c*-axis thermal diffusivity of PRGP and GOP. (b) Classic laser flash characterization of PRGP at RT.

PRGP. This $k_c$ value exceeds the low bound of the amorphous limit (about $1–2$ W m$^{-1}$ K$^{-1}$) [49, 50]. Such unprecedented low cross-plane thermal conductivity has been reported by Chiritescu *et al* [51]. In their work, Chiritescu reported a thermal conductivity of $0.05$ W m$^{-1}$ K$^{-1}$ at RT for a fully dense disordered and layered thin WSe$_2$ film. This value is 30 times smaller than $k_c$ of single-crystallite WSe$_2$ layered structure and 6 times smaller than the predicted minimum thermal conductivity for this material. The author attributed the extremely low $k_c$ to the localization of lattice vibrations induced by the random stacking 2D WSe$_2$ sheets. This may also be a reason for the low $k_c$ in our PRGP which is also assembled by layered, disordered rGO sheets.

### 3.2. Thermal diffusivity analysis

Note that, $c_p$ is a key parameter in the calculation or fitting of $k_c$, as the PLTR2 technique is based on the thermal diffusivity measurement. As described before, $c_p$ of PRGP and GOP are taken from that of graphite, while the discrepancy from graphite is unclear. Although we have performed direct DSC measurement of $c_p$, the available data is only at near RT. The discrepancy of $c_p$ is mainly from different interlayer coupling strength and different chemical bonds other than the C–C sp$^2$ bonds in pristine graphite. The interlayer coupling strength is directly related to the interlayer spacing which will get weaker as the interlayer spacing increases. Thus, the discrepancy of the GOP from graphite may be relatively larger due to the large interlayer spacing ($8.4$ Å). This discrepancy is weak at high temperature as the heat capacity is mainly from the contribution of high-frequency phonons in the in-plane direction. However, as temperature decrease, the high-frequency phonons will get frozen and the long wavelength phonons with strong interlayer coupling will be more significant. Different chemical bonds other than the C–C sp$^2$ bonds are more likely to induce significant discrepancy in $c_p$.

The bonding energy introduced by the other bonds like the C–O is different from that of the C–C sp$^2$ bonds. Moreover, the oxygen atoms attached to the C atoms will convert the C–C sp$^2$ bonds to sp$^3$ bonds. This conversion has been confirmed by Mkhoyan [52], where a 1:5 oxygen to carbon atoms ratio could lead to 40% of the sp$^2$ bonds into sp$^3$ bonds. Thus, $c_p$ of PRGP and GOP may have significant discrepancy from those of graphite, especially for GOP with much higher oxygen component.

Therefore, with the unknown discrepancy of $c_p$ and the difference in density, the uncertainty of $k_c$ may be large. In this case, we will mainly focus on $\alpha_c$, the cross-plane thermal diffusivity in interpreting the thermal transport in PRGP and GOP in the following sections. For GOP, $\alpha_c$ can be directly derived from the half rise time $t_{1/2}$, as described before. The derived $\alpha_c$ is shown in figure 6(a), which varies from $(1.52 \pm 0.05) \times 10^{-7}$ m$^2$ s$^{-1}$ at 295 K to $(2.28 \pm 0.08) \times 10^{-7}$ m$^2$ s$^{-1}$ at 12.5 K. For PRGP, the measurement is performed on the multilayered PRGP/PMMA/PET/Ir film, and the thermal conductivity is first derived from the least square fitting. Then the thermal diffusivity is calculated as $k = \alpha \cdot \rho \cdot c_p$. Additional fitting processes are performed with $c_p$ varies around the value of graphite. The results show that the fitted $k_c$ changes proportionally to the variation of $c_p$. In contrast, the calculated $\alpha_c$ varies no larger than 10% even the deviation of $c_p$ reaches 100%. This is, however, expected for the PLTR2 model as it is based on the thermal diffusivity measurement. Therefore, the measured thermal diffusivity has a low uncertainty and can be used to better analyze the thermal transport in the sample in this work. From figure 6(a) we can see $\alpha_c$ of PRGP ranges from $(1.02 \pm 0.09) \times 10^{-7}$ m$^2$ s$^{-1}$ at 295 K to $(2.31 \pm 0.18) \times 10^{-7}$ m$^2$ s$^{-1}$ at 12 K, showing an increasing trend as temperature decreases, like those of GOP and GP. $\alpha_c$ of PRGP have no significant difference for the down round and up round measurements at a given experimental temperature. This means the low

temperature has negligible influence on the structure of PRGP, or at least the PRGP has no irreversible structure changes during the low-temperature process. The uncertainties in the determined $\alpha_c$ of PRGP and GOP come from the errors in the determination of the thicknesses and the fitting process.

To confirm the measurement accuracy of the PLTR2 technique on the multilayered sample, the classical laser flash method is applied on PRGP at RT. In this measurement, the PRGP is suspended, with no PET or PMMA films attached, no Ir coating. The same nanosecond pulsed laser is used to heat the front surface of the sample. The temperature at the back surface is detected by an infrared detector, which is connected to a pre-amplifier and then to the oscilloscope. Figure 6(b) shows the temperature evolution curve at the front surface. The half rise time is 145 $\mu$s, from which the thermal diffusivity at RT is calculated at $1.27 \times 10^{-7}\,\mathrm{m^2\,s^{-1}}$ with $\alpha = (1.37 L^2/\pi^2 t_{1/2})$. This value is about 25% larger than that determined from the PLTR2 measurement, but still proves the measurement accuracy of the PLTR2 technique on the multilayered sample considering some sample-to-sample structure difference. The difference may come from the uncertainty in the thicknesses of the PMMA and PET. The different environments may be another reason. Not like the PLTR2 technique, this laser flash measurement is performed in the atmosphere with no vacuum or temperature control. In this case, the convection may also lead to errors in the results. In this classic laser flash method, the thermal diffusivity can be directly derived, without additional process of the sample or fitting of the experimental. However, the infrared detector cannot work well at very low temperatures and cannot be put into our vacuum chamber. Therefore, we developed the PLTR2 technique and performed the measurement from RT down to very low temperatures in a well temperature and vacuum controlled system to uncover the structure and thermal transport properties evolution against temperature.

## 4. Physical interpretation of the low $\alpha_c$ of PRGP and GOP

Thermal transport in carbon-based materials are dominated by phonons from lattice vibrations and the contribution of electrons is negligible [45, 53]. This also holds true for PRGP and GOP. The phonon thermal conductivity can be expressed by the following equation [54]:

$$k_p = \sum_j \int C_j(\omega)\, v_j^2(\omega)\, \tau_j(\omega)\, \mathrm{d}\omega, \qquad (4)$$

where $\omega$ is the phonon frequency; $C_j$ the contribution to heat capacity from the $j$th branch; $v_j = \mathrm{d}\omega_j/\mathrm{d}q$ the phonon group velocity of the $j$th branch; $\tau_j$ the phonon relaxation time. For 1D thermal transport, this equation can be simplified as $k_p = Cvl$, taking the average phonon group velocity ($v$) and phonon mean free path (MFP noted as $l$) for all the phonon branches. The thermal diffusivity is defined as $\alpha = k/C$, so we have $\alpha = vl$. In general, we can see that the thermal diffusivity is proportional to the phonon group velocity and

the phonon MFP. For PRGP, the phonon MFP is limited by phonon scattering from the defects and grain boundaries as described in the last section. Thus, the phonon MFP should be smaller than the crystallite size. From the XRD characterization, the crystallite size is determined at 4.8 nm. This value is more than one order of magnitude smaller than that of GP (234 nm) determined in our recent work [17] and is also tens of times smaller than that of graphite (at the hundred-nm scale) reported in other work [18, 19, 55]. This small crystallite size will induce intensive phonon scattering at the grain boundaries and defect spots which is the main reason for the low $\alpha_c$ of PRGP compared with GP or graphite.

The relatively larger interlayer spacing of PRGP (3.68 Å) compared with GP and highly ordered graphite (3.35 Å) may be another factor that suppresses $\alpha_c$ of PRGP. The enlargement of interlayer spacing changes the phonon dispersion and the interlayer binding energy where the energy coupling of interlayer atoms through van der Waals force will get weaker [56, 57]. In this case, fewer phonon modes will be activated and occupied in the thermal transport in the cross-plane direction. Moreover, as the interlayer spacing gets larger, the cross-plane phonon group velocity will also be reduced and lead to the decrease of $\alpha_c$, according to the equation $\alpha = vl$. The functional groups may also play a role in the reduction of $\alpha_c$ in PRGP. However, the interlayer spacing is 3.68 Å from the XRD results, only 10% larger than that of highly ordered graphite. This means few atoms or oxygen-contained functional groups (mostly hydroxyl and epoxy groups) exist on the basal plane and most of the functional groups (mostly carboxylic acid and other groups like ketones) are located at the edges of the graphene sheets [15, 26]. Figure 7(a) shows a schematic illustration of the PRGP layered structure. The accumulated functional groups at the sheet edges may enhance the boundary scattering which will also suppress the thermal transport in the cross-plane direction. The existence of Iodine (I) atoms may be another reason. According to the EDS results, the atomic fraction of I in the PRGP is about 3.65%. These I atoms may come from the reduction process which use HI acid to perform the chemical reduction to produce rGO from GO. The I atom can provide significant scattering sources due to its heavy mass. Also, there may be some vacancies and distortions existing in the basal plane due to the removal of carbon atoms upon chemical reduction [24]. This kind of defects also serve as scattering sources and weakens the energy coupling in the cross-plane direction.

For GOP, $\alpha_c$ is also much smaller than that of GP and graphite. The crystallite size of GOP is determined at 7.1 nm from XRD, tens of times smaller than that of GP and highly ordered graphite as described before. Like in the PRGP, the small crystallite size also suppresses $\alpha_c$ of GOP significantly. The interlayer spacing is determined at 8.4 Å from the XRD study, much larger than that in GP, PRGP, and graphite. In this case, direct energy coupling between carbon layers through van der Waals force is reduced to a negligible level. The relation between the interlayer spacing and the binding energy among layers of graphite has been theoretically studied by Spanu [56] and Chen [57]. In Spanu's work, an *ab initio* many-body theory was used to compute the
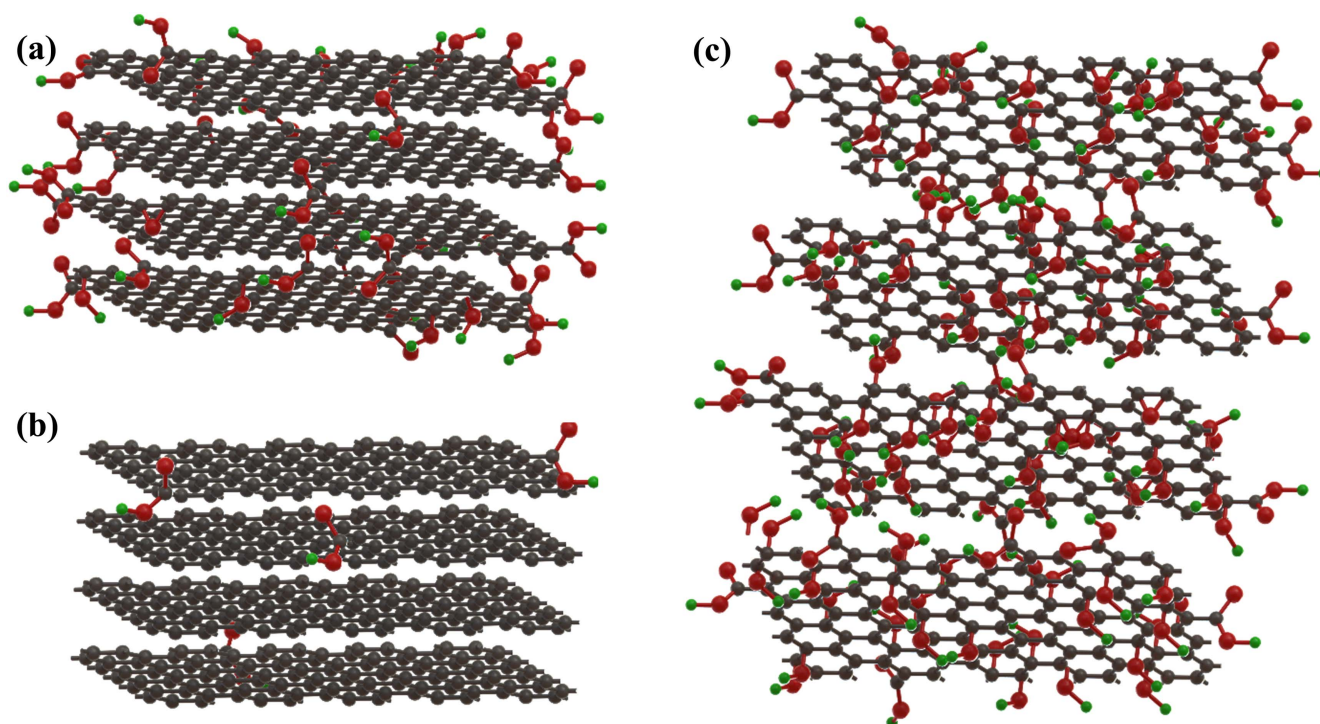
**Figure 7.** Schematic illustration of the samples. (not to scale) Gray: carbon atoms; red: oxygen atoms; green: hydrogen atoms (a) PRGP with an interlayer spacing of 3.68 Å. (b) GP with an interlayer spacing of 3.35 Å. (c) GOP with an interlayer spacing of 8.4 Å.

interlayer bonding properties of graphite. The results showed that the binding energy rises when the interlayer spacing is larger than 3.35 Å and approaches zero when it is larger than 7 Å. Similarly, in Chen' work, the interlayer potentials and interlayer binding energy of graphite were calculated as a function of the interlayer spacing by using a modified Mobius method based on *ab initio* calculations. The result shows that when the interlayer spacing is larger than 8 Å, the interlayer potentials and the interlayer banding energy are negligible [57]. Nevertheless, $\alpha_c$ of GOP is comparable or even larger than that of PRGP. This means other mechanisms should exist and support the weak thermal transport in the cross-plane direction. The existence of functional groups on the basal plane is probably one of the major reason. Not like the PRGP which has smaller interlayer spacing and hold few atoms or functional groups in the basal plane, the GOP has an interlayer spacing of 8.4 Å, large enough to hold those functional groups like epoxy and hydroxyl among layers [25], and even functional chains that connect the graphene layers. The EDS study also shows that the GOP contains more Oxygen than PRGP (atomic fraction of 35.12% and 9.93% for GOP and PRGP, respectively). Previous work by Gao *et al* [58] shows that the oxygen-contained functional groups on the basal plane are easier to remove upon chemical reduction, as expected for PRGP. Compared with PRGP, the existence of functional groups on the basal plane provides additional exfoliation energy which helps keep the PRGP stable.

The existence of functional groups will destruct the graphene conjugated structure and lead to the decrease of electrical conductivity and thermal transport. This is also the main reason that the in-plane thermal conductivity of GOP

and PRGP are orders of magnitude lower than that of GP and graphite. The functional groups are most likely non-conductive and their existence will reduce thermal transport of GOP and PRGP in the cross-plane direction. Despite the much lower cross-plane thermal conductivity/diffusivity in GOP and PRGP than in GP, the behind mechanism may be different. In PRGP, the interlayer spacing is about 10% larger than that of GP and graphite. The inter-graphene layer van der Waals force is still strong enough and sustains thermal transport in the cross-plane direction. While in GOP, the interlayer spacing is about 8.4 Å, where direct energy coupling among graphene layers through van der Waals force is reduced to a negligible level. In this case, the functional groups and chains provide tunnels, although very weak, that support thermal transport in the cross-plane direction. In other words, thermal transport across the GOP sample need to be via the functional groups between graphene layers in the absence of direct energy coupling. Figure 7(c) shows a schematic illustration of the GOP structure. Compared with figure 7(a) of PRGP, we can see there are much more functional groups held on the basal plane in GOP.

For comparison, a schematic illustration of the GP structure studied in our previous work [17] is also shown in figure 7(b). From the EDS study, the atomic fraction of the existing elements in GP is carbon (99.81%), oxygen (0.19%), indicating a high purified carbon material. In addition, the XRD characterization also showed that the interlayer spacing of GP is 3.35 Å, the same as highly ordered graphite. Thus, we believe that the GP has almost the same structure as that of highly ordered graphite, where few defects exist in the basal plane or at the edges of graphene sheet (as shown in

figure 7(b)). The thermal transport properties of GP have also been characterized in our previous work [16, 17]. The results show that $k_a$ is about $600\,W\,m^{-1}\,K^{-1}$ at RT and switch to $3200\,W\,m^{-1}\,K^{-1}$ at about 245 K and $k_c$ is about $6\,W\,m^{-1}\,K^{-1}$, close to those of highly ordered graphite. This also proves that GP is composed of highly purified and ordered graphene sheets. As a result, we can claim that the low $k_c$ and $\alpha_c$ of PRGP is due to its unique structure compared with the GP. The combined effects from the small grain size, the large interlayer spacing and the high-level defects such as functional groups, vacancies, and distortions lead to the significant reduction of $\alpha_c$ in PRGP. As detailed before, for GOP, a large number of functional groups are located on the basal plane, while for PRGP, the remaining functional groups are at the edges of the graphene flakes. The different locations of functional groups also have strong effects on the thermal transport properties of those graphene-based materials.

This work sheds light on future work on graphene-based thermal interface materials and thermal management. The effect of the type and quantity of functional groups on thermal conductivity and diffusivity is an interesting and challenging aspect of future study. In the near future, the thermal conductivity/diffusivity in the cross-plane direction varying with the annealing level will be further investigated by applying thermal annealing to the PRGP and GOP and varying the annealing temperatures and speed. The interlayer spacing and the grain size in the cross-plane direction against the annealing temperature will be an interesting topic to be studied. In addition, the large in-plane thermal conductivity of graphene-based paper is highly favorable in reducing the local hot spot temperature and the possibility of thermal failure. The combined effect of thermal interface enhancement and the lateral heat spreading of graphene-based papers will be further investigated.

## 5. Conclusion

In this work, the thermal transport properties of PRGP and GOP in the cross-plane direction are characterized using a pulsed laser-assisted thermal relaxation 2 (PLTR2) technique from RT down to 12 K. For PRGP, the measurement was taken within a cycled temperature variation, including a down-round from 295 K down to 12 K and an up-round from 12 K back to 295 K. $k_c$ ranges from $0.14\,W\,m^{-1}\,K^{-1}$ at 295K to $1.2 \times 10^{-3}\,W\,m^{-1}\,K^{-1}$ at 12 K, with no significant difference between the two rounds. For GOP, $k_c$ decreases from $0.16\,W\,m^{-1}\,K^{-1}$ at 295 K down to $9.7 \times 10^{-4}\,W\,m^{-1}\,K^{-1}$ at 12.5 K, which is very similar to those of PRGP. To eliminate the influence of heat capacity of different structures, the thermal diffusivity was further studied. In contrary to $k_c$, $\alpha_c$ of PRGP increases from $(1.02 \pm 0.09) \times 10^{-7}\,m^2\,s^{-1}$ at 295 K to $(2.31 \pm 0.18) \times 10^{-7}\,m^2\,s^{-1}$ at 12 K. Such small $\alpha_c$ is mainly attributed to the small crystallite size (4.8 nm from XRD) in the cross-plane direction. The larger interlayer spacing (3.68 Å compared with 3.35 Å of GP) is another reason. For GOP, $\alpha_c$ varies from $(1.52 \pm 0.05) \times 10^{-7}\,m^2\,s^{-1}$ at 295

K to $(2.28 \pm 0.08) \times 10^{-7}\,m^2\,s^{-1}$ at 12.5 K, also tens of times smaller than those of GP or graphite. Different from PRGP, GOP has a much larger interlayer spacing (8.4 Å), which makes the direct energy coupling between layers negligible. The high density of functional groups like hydroxyl and epoxy on the basal plane provide additional forces that hold the material stable and support the weak thermal transport across the carbon layers. The result of this work provides fundamental guidance for graphene-based paper structure control and thermal design toward novel thermal interface applications.

## Acknowledgments

## ORCID iDs

Meng Han ⓘ https://orcid.org/0000-0003-4763-5559
Jingchao Zhang ⓘ https://orcid.org/0000-0001-5289-6062

## References

[1] Novoselov K S, Geim A K, Morozov S V, Jiang D, Zhang Y, Dubonos S V, Grigorieva I V and Firsov A A 2004 Electric field effect in atomically thin carbon films *Science* **306** 666–9

[2] Balandin A A, Ghosh S, Bao W Z, Calizo I, Teweldebrhan D, Miao F and Lau C N 2008 Superior thermal conductivity of single-layer graphene *Nano Lett.* **8** 902–7

[3] Klemens P and Pedraza D 1994 Thermal conductivity of graphite in the basal plane *Carbon* **32** 735–41

[4] Cai W, Moore A L, Zhu Y, Li X, Chen S, Shi L and Ruoff R S 2010 Thermal transport in suspended and supported monolayer graphene grown by chemical vapor deposition *Nano Lett.* **10** 1645–51

[5] Seol J H, Jo I, Moore A L, Lindsay L, Aitken Z H, Pettes M T, Li X, Yao Z, Huang R and Broido D 2010 Two-dimensional phonon transport in supported graphene *Science* **328** 213–6

[6] Hu H, Zhao Z, Wan W, Gogotsi Y and Qiu J 2013 Ultralight and highly compressible graphene aerogels *Adv. Mater.* **25** 2219–23

[7] Xie Y, Xu S, Xu Z, Wu H, Deng C and Wang X 2016 Interface-mediated extremely low thermal conductivity of graphene aerogel *Carbon* **98** 381–90

[8] Xie Y, Xu Z, Xu S, Cheng Z, Hashemi N, Deng C and Wang X 2015 The defect level and ideal thermal conductivity of graphene uncovered by residual thermal reffusivity at the 0 K limit *Nanoscale* **7** 10101–10

[9] Zhao Y, Liu J, Hu Y, Cheng H, Hu C, Jiang C, Jiang L, Cao A and Qu L 2013 Highly compression-tolerant supercapacitor based on polypyrrole-mediated graphene foam electrodes *Adv. Mater.* **25** 591–5

[10] Xin G, Sun H, Hu T, Fard H R, Sun X, Koratkar N, Borca-Tasciuc T and Lian J 2014 Large-area freestanding graphene paper for superior thermal management *Adv. Mater.* **26** 4521–6

[11] Renteria J D, Ramirez S, Malekpour H, Alonso B, Centeno A, Zurutuza A, Cocemasov A I, Nika D L and Balandin A A 2015 Strongly anisotropic thermal conductivity of free-standing reduced graphene oxide films annealed at high temperature *Adv. Funct. Mater.* **25** 4664–72

[12] Xiang J and Drzal L T 2011 Thermal conductivity of exfoliated graphite nanoplatelet paper *Carbon* **49** 773–8

[13] Wu H and Drzal L T 2012 Graphene nanoplatelet paper as a light-weight composite with excellent electrical and thermal conductivity and good gas barrier properties *Carbon* **50** 1135–45

[14] Malekpour H, Chang K-H, Chen J-C, Lu C-Y, Nika D, Novoselov K and Balandin A 2014 Thermal conductivity of graphene laminate *Nano Lett.* **14** 5155–61

[15] Song N-J, Chen C-M, Lu C, Liu Z, Kong Q-Q and Cai R 2014 Thermally reduced graphene oxide films as flexible lateral heat spreaders *J. Mater. Chem.* A **2** 16563–8

[16] Xie Y, Yuan P, Wang T, Hashemi N and Wang X 2016 Switch on the high thermal conductivity of graphene paper *Nanoscale* **8** 17581–97

[17] Han M, Liu J, Xie Y and Wang X 2018 Sub-$\mu$m *c*-axis structural domain size of graphene paper uncovered by low-momentum phonon scattering *Carbon* **126** 532–43

[18] Fu Q, Yang J, Chen Y, Li D and Xu D 2015 Experimental evidence of very long intrinsic phonon mean free path along the *c*-axis of graphite *Appl. Phys. Lett.* **106** 031905

[19] Zhang H, Chen X, Jho Y-D and Minnich A J 2016 Temperature-dependent mean free path spectra of thermal phonons along the *c*-axis of graphite *Nano Lett.* **16** 1643–9

[20] Hirata M, Gotou T, Horiuchi S, Fujiwara M and Ohba M 2004 Thin-film particles of graphite oxide 1:: high-yield synthesis and flexibility of the particles *Carbon* **42** 2929–37

[21] Hummers W S Jr and Offeman R E 1958 Preparation of graphitic oxide *J. Am. Chem. Soc.* **80** 1339

[22] Chen H, Müller M B, Gilmore K J, Wallace G G and Li D 2008 Mechanically strong, electrically conductive, and biocompatible graphene paper *Adv. Mater.* **20** 3557–61

[23] Liu J, Wang R, Cui L, Tang J, Liu Z, Kong Q, Yang W and Gooding J 2012 Using molecular level modification to tune the conductivity of graphene papers *J. Phys. Chem.* C **116** 17939–46

[24] Chen C-M, Huang J-Q, Zhang Q, Gong W-Z, Yang Q-H, Wang M-Z and Yang Y-G 2012 Annealing a graphene oxide film to produce a free standing high conductive graphene film *Carbon* **50** 659–67

[25] Botas C, Álvarez P, Blanco C, Santamaría R, Granda M, Gutiérrez M D, Rodríguez-Reinoso F and Menéndez R 2013 Critical temperatures in the synthesis of graphene-like materials by thermal exfoliation–reduction of graphite oxide *Carbon* **52** 476–85

[26] Vallés C, Núñez J D, Benito A M and Maser W K 2012 Flexible conductive graphene paper obtained by direct and gentle annealing of graphene oxide paper *Carbon* **50** 835–44

[27] Park S, An J, Potts J R, Velamakanni A, Murali S and Ruoff R S 2011 Hydrazine-reduction of graphite-and graphene oxide *Carbon* **49** 3019–23

[28] Johra F T, Lee J-W and Jung W-G 2014 Facile and safe graphene preparation on solution based platform *J. Ind. Eng. Chem.* **20** 2883–7

[29] Shin H J, Kim K K, Benayad A, Yoon S M, Park H K, Jung I S, Jin M H, Jeong H K, Kim J M and Choi J Y 2009 Efficient reduction of graphite oxide by sodium borohydride and its effect on electrical conductance *Adv. Funct. Mater.* **19** 1987–92

[30] Stankovich S, Dikin D A, Piner R D, Kohlhaas K A, Kleinhammes A, Jia Y, Wu Y, Nguyen S T and Ruoff R S 2007 Synthesis of graphene-based nanosheets via chemical reduction of exfoliated graphite oxide *Carbon* **45** 1558–65

[31] Pei S, Zhao J, Du J, Ren W and Cheng H-M 2010 Direct reduction of graphene oxide films into highly conductive and flexible graphene films by hydrohalic acids *Carbon* **48** 4466–74

[32] Tuinstra F and Koenig J L 1970 Raman spectrum of graphite *J. Chem. Phys.* **53** 1126–30

[33] Gurzęda B, Florczak P, Wiesner M, Kempiński M, Jurga S and Krawczyk P 2016 Graphene material prepared by thermal reduction of the electrochemically synthesized graphite oxide *RSC Adv.* **6** 63058–63

[34] Chen C-M, Zhang Q, Yang M-G, Huang C-H, Yang Y-G and Wang M-Z 2012 Structural evolution during annealing of thermally reduced graphene nanosheets for application in supercapacitors *Carbon* **50** 3572–84

[35] Ferrari A C, Meyer J, Scardaci V, Casiraghi C, Lazzeri M, Mauri F, Piscanec S, Jiang D, Novoselov K and Roth S 2006 Raman spectrum of graphene and graphene layers *Phys. Rev. Lett.* **97** 187401

[36] Moon I K, Lee J, Ruoff R S and Lee H 2010 Reduced graphene oxide by chemical graphitization *Nat. Commun.* **1** 73

[37] Hohenauer W and Vozár L 2001 An estimation of thermophysical properties of layered materials by the laser-flash method *High Temp.-High Press.* **33** 17–26

[38] Parker W, Jenkins R, Butler C and Abbott G 1961 Flash method of determining thermal diffusivity, heat capacity, and thermal conductivity *J. Appl. Phys.* **32** 1679–84

[39] Lee H J 1975 *Thermal Diffusivity in Layered and Dispersed Composites* (Lafayette, IA: Purdue University) 7600554

[40] Dainton F, Evans D M, Hoare F and Melia T 1962 Thermodynamic functions of linear high polymers: part I — polyoxymethylene *Polymer* **3** 263–321

[41] Barron T and White G K 2012 *Heat Capacity and Thermal Expansion at Low Temperatures* (New York: Springer)

[42] DeSorbo W and Tyler W 1953 The specific heat of graphite from 13 to 300 K *J. Chem. Phys.* **21** 1660–3

[43] Naik G and Krishnaswamy S 2017 Photoreduction and thermal properties of graphene-based flexible films *Graphene* **6** 27

[44] Mahanta N K and Abramson A R 2012 Thermal conductivity of graphene and graphene oxide nanoplatelets *13th Intersociety Conf. on Thermal and Thermomechanical Phenomena in Electronic Systems* (San Diego: IEEE) pp 1–6

[45] Pop E, Varshney V and Roy A K 2012 Thermal properties of graphene: fundamentals and applications *MRS Bull.* **37** 1273–81

[46] Choy C L 1977 Thermal-conductivity of polymers *Polymer* **18** 984–1004

[47] Choy C and Greig D 1977 The low temperature thermal conductivity of isotropic and oriented polymers *J. Phys. C: Solid State Phys.* **10** 169

[48] Pohl R O, Liu X and Thompson E 2002 Low-temperature thermal conductivity and acoustic attenuation in amorphous solids *Rev. Mod. Phys.* **74** 991–1013

[49] Cahill D G, Watson S K and Pohl R O 1992 Lower limit to the thermal conductivity of disordered crystals *Phys. Rev.* B **46** 6131

[50] Bullen A J, O'Hara K E, Cahill D G, Monteiro O and von Keudell A 2000 Thermal conductivity of amorphous carbon thin films *J. Appl. Phys.* **88** 6317–20

[51] Chiritescu C, Cahill D G, Nguyen N, Johnson D, Bodapati A, Keblinski P and Zschack P 2007 Ultralow thermal conductivity in disordered, layered $WSe_2$ crystals *Science* **315** 351–3

[52] Mkhoyan K A, Contryman A W, Silcox J, Stewart D A, Eda G, Mattevi C, Miller S and Chhowalla M 2009 Atomic and electronic structure of graphene-oxide *Nano Lett.* **9** 1058–63

[53] Nihira T and Iwata T 2003 Temperature dependence of lattice vibrations and analysis of the specific heat of graphite *Phys. Rev.* B **68** 134305

[54] Nika D L and Balandin A A 2012 Two-dimensional phonon transport in graphene *J. Phys. Condens.: Matter* **24** 233203

[55] Wei Z, Yang J, Chen W, Bi K, Li D and Chen Y 2014 Phonon mean free path of graphite along the *c*-axis *Appl. Phys. Lett.* **104** 081903

[56] Spanu L, Sorella S and Galli G 2009 Nature and strength of interlayer binding in graphite *Phys. Rev. Lett.* **103** 196401

[57] Chen X, Tian F, Persson C, Duan W and Chen N-X 2013 Interlayer interactions in graphites *Sci. Rep.* **3** 3046

[58] Gao X, Jang J and Nagase S 2009 Hydrazine and thermal reduction of graphene oxide: reaction mechanisms, product structures, and reaction design *J. Phys. Chem.* C **114** 832–42